

Relationship between polyhedral structures formed by tangent planes of ellipsoidal particles and system sound velocity

Cheng-Bo Li(李成波), Lin Bao(鲍琳), and Chuang Zhao(赵闯)

Citation: Chin. Phys. B, 2024, 33 (**11**): 118301. DOI: 10.1088/1674-1056/ad7726
Journal homepage: http://cpb.iphy.ac.cn; http://iopscience.iop.org/cpb

What follows is a list of articles you may be interested in

A pressure-sensitive rheological origin of high friction angles of granular matter observed in NASA-MGM project

Xiaohui Cheng(程晓辉), Shize Xiao(肖世泽), Sen Yang(杨森), Naifeng Zhao(赵乃峰), and Alex Sixie Cao
Chin. Phys. B, 2024, 33 (**6**): 068301. DOI: 10.1088/1674-1056/ad3b88

Nonlinear interaction of head-on solitary waves in integrable and nonintegrable systems

Shutian Zhang(张树甜), Shikun Liu(刘世鲲), Tengfei Jiao(矫滕菲), Min Sun(孙敏), Fenglan Hu(胡凤兰), and Decai Huang(黄德财)
Chin. Phys. B, 2024, 33 (**5**): 054501. DOI: 10.1088/1674-1056/ad1dcb

Effect of granular shape on radial segregation in a two-dimensional drum

Yue Xu(徐悦), Ran Li(李然), Zhipeng Chi(迟志鹏), Wenzheng Xiu(修文正), Qicheng Sun(孙其诚), and Hui Yang(杨晖)
Chin. Phys. B, 2024, 33 (**4**): 044502. DOI: 10.1088/1674-1056/ad1092

Numerical simulation for the initial state of avalanche in polydisperse particle systems

Ren Han(韩韧), Ting Li(李亭), Zhipeng Chi(迟志鹏), Hui Yang(杨晖), and Ran Li(李然)
Chin. Phys. B, 2024, 33 (**2**): 024501. DOI: 10.1088/1674-1056/ad117b

Resistance law of a rod penetrating a multilayer granular raft

Zonglin Li(李宗霖), Qiang Tian(田强), and Haiyan Hu(胡海岩)
Chin. Phys. B, 2023, 32 (**3**): 034501. DOI: 10.1088/1674-1056/aca5ff

---

Relationship between polyhedral structures formed by tangent planes of ellipsoidal particles and system sound velocity

Cheng-Bo Li(李成波)[1], Lin Bao(鲍琳)[2], and Chuang Zhao(赵闯)[2,†]

[1] *School of Materials Science and Engineering, Anyang Institute of Technology, Anyang* 455000, *China*
[2] *College of Physics, Guizhou University, Guiyang* 550025, *China*

(Received 8 July 2024; revised manuscript received 22 August 2024; accepted manuscript online 4 September 2024)

Internal polyhedral structures of a granular system can be investigated using the Voronoi tessellations. This technique has gained increasing recognition in research of kinetic properties of granular flows. For systems with mono-sized spherical particles, Voronoi tessellations can be utilized, while radial Voronoi tessellations are necessary for analyzing systems with multi-sized spherical particles. However, research about polyhedral structures of non-spherical particle systems is limited. We utilize the discrete element method to simulate a system of ellipsoidal particles, defined by the equation $(\frac{x}{\alpha})^2+(\frac{y}{1})^2+(\frac{z}{1/\alpha})^2=1$, where α ranges from 1.1 to 2.0. The system is then dissected by using tangent planes at the contact points, and the geometric quantities of the resulting polyhedra in different shaped systems, such as surface area, volume, number of vertices, number of edges, and number of faces, are calculated. Meanwhile, the longitudinal and transverse wave velocities within the system are calculated with the time-of-flight method. The results demonstrate a strong correlation between the sound velocity of the system and the geometry of the dissected polyhedra. The sound velocity of the system increases with the increase in α, peaking at $\alpha=1.3$, and then decreases as α continues to increase. The average volume, surface area, number of vertices, number of edges, and number of faces of the polyhedra decrease with the increase in sound velocity. That is, these quantities initially decrease with the increase in α, reaching minima at $\alpha=1.3$, and then increase with further increase of α. The relationship between sound velocity and the geometric quantities of the dissected polyhedra can serve as a reference for acoustic material design.

Keywords: discrete element method, Voronoi tessellation, polyhedral structure, sound velocity

PACS: 45.70.–n, 46.40.Cd, 83.80.Fg **DOI:** 10.1088/1674-1056/ad7726

1. Introduction

A multitude of particle systems exist in nature and industrial processes, including soils, pharmaceuticals, and building materials, etc. Research of properties of particle systems holds significant scientific importance and substantial application value. The macroscopic mechanical properties of a system are reflections of its microstructure. Consequently, explaining macroscopic properties from the perspective of microstructure analysis is increasingly valued. Among these methods, Voronoi analysis is a commonly employed approach.[1]

A Voronoi tessellation polyhedron is defined as a region composed of points whose distance from a given point is less than or equal to their distance from other discrete points. This model is of significant importance, and numerous problems can be formulated in such a manner for research purposes. For instance, crystals, colloids, and the universe can all be conceptualized as collections of point-like objects in space.[1] This raises the problem of whether the organizational form of the elements (atoms, colloidal particles, and celestial bodies) that constitute these physical systems is ordered or disordered. If the structure is ordered, it would be beneficial to determine how defects are classified and how they affect the properties of the system. What is the most effective method for characterizing the disordered state of systems such as liquids, glass, or particulate matter? Addressing these fundamental questions is inextricably linked to examining the polyhedral structures created by Voronoi tessellations. Voronoi tessellation is not merely a tool for solving specific mathematical and engineering problems. It is also an effective means of understanding and analyzing complex systems.

The analysis of the topological structure and kinetic properties of amorphous systems, such as granular matter, also heavily relies on Voronoi tessellation. This method is essential because Voronoi tessellation can accurately characterize the local volume fraction within the system. The local volume fraction of an individual particle can be precisely determined by dividing its volume by the volume of the Voronoi tessellation polyhedron that surrounds the particle.

This method allows for highly accurate analysis of volume fractions at the particle scale. Such precision is crucial for studying kinetic properties of granular systems, as fluctuations in volume fraction of a few percentages can have a significant impact on the mechanical properties of the system.[1] Furthermore, phase transitions such as jamming and unjamming are closely tied to subtle variations in volume fraction. In nuclear reactors, the flow characteristics of spherical graphite particles are intricately linked to local volume fractions,[2] making the precise determination of these fractions through Voronoi tes-

†Corresponding author. E-mail: 1508868030@qq.com

© 2024 Chinese Physical Society and IOP Publishing Ltd

sellation crucial for designing reactor feed supply systems.[3,4]

The discrete element method (DEM) provides a convenient approach for calculating the volume of Voronoi tessellation polyhedra and the local volume fraction of individual particles. The combination of these two methods has emerged as a powerful tool for studying kinetic properties of particle systems. Furthermore, applications of Voronoi analysis enable identifications of numerous distinctive properties of granular systems. As an example, the local volume fraction variance decreases consistently as the system density increases, a trend unaffected by boundary conditions or friction coefficients.[5] Moreover, in systems under shear, Voronoi tessellation-based calculations of local volume fraction uncover the emergence of two bands with lower packing fractions at the shear boundary. In these areas, particles exhibit distinct motion patterns, requiring slight separation to facilitate their movement. Such analyses provide a fundamental basis for exploring the mechanics of granular systems.[6]

In addition to determining local volume fractions, Voronoi tessellation polyhedra are employed extensively in studying granular and other amorphous systems to identify neighboring particles[7] and investigate system anisotropy.[8,9] Voronoi tessellation is also crucial for quantitatively analyzing pore characteristics within granular systems,[5,10] where pore features at the particle scale are closely linked to deformation behavior, stress distribution, and conductivity.[11–15] Furthermore, Voronoi tessellation plays a pivotal role in assessing internal structure and mechanical properties of these systems.

The Voronoi tessellation method has specific prerequisites for studying particle systems. It is suitable for spherical particle systems of a uniform size, whereas radial Voronoi tessellation is employed for multi-dispersion spherical systems. Non-spherical particle systems exhibit complex Voronoi tessellations, with tessellation units typically surrounded by irregularly shaped surfaces. Consequently, there has been relatively limited exploration of non-spherical particle systems using this method.[16–19]

This study utilizes the DEM to simulate ellipsoidal systems, by employing the tangent plane at the contact point to generate polyhedrons. Geometric quantities of the polyhedrons in various shape systems, such as surface area, volume, number of vertices, edges, and faces, are computed.

In contrast, the anisotropic internal structure induced by shape will manifest itself in changes to the macroscopic mechanical properties. For instance, different local structures will influence the velocity, attenuation, and dispersion of elastic waves.[20,21] The relationship between internal structure and sound velocity is of great importance for the determination of force chain distribution, anisotropic behavior,[21–25] formation of shear bands,[26] and even collapse processes.[27] Consequently, the influence of particle shape on sound velocity has become a subject of considerable research interest. The effect of shape on sound velocity is primarily examined by investigating how aspect ratio and blockiness of particles change,[28] or how particle angularity influences systems' properties and then affects sound velocity.[29,30] Nevertheless, research on the effect of polyhedral particle geometry on sound velocity is limited.

To explore the relationship between geometric structure and macroscopic acoustic properties, the propagation of sound within the particle system is simulated, and sound velocity is calculated. A correlation between the structure of dissected polyhedrons and system sound velocity is identified, providing insights into macroscopic properties from a micro geometric perspective.

2. Simulations, sound velocities and dissected polyhedra

In this section, the DEM is employed to simulate the packing of ellipsoidal particle systems of varying shapes under different normal stresses. After the system reaches equilibrium under these stresses, the propagation of elastic waves within the system is simulated using harmonic vibration, and the sound velocity is calculated. Finally, the method for computing dissected polyhedra is introduced.

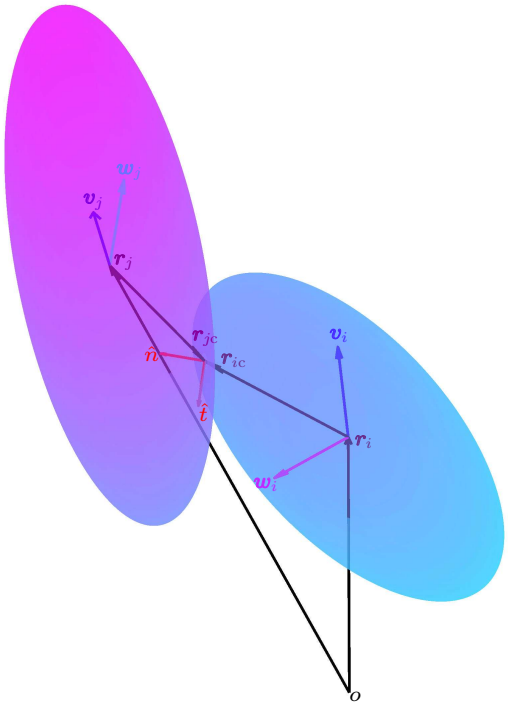


Fig. 1. Geometrical relations and physical quantities of contact particles.

2.1. Contact model

The methodology to determine contact points between ellipsoidal particles follows established procedures documented in the literature.[31,32] This approach enables the determination of key geometric parameters, including effective radius, normal vector, and contact point overlap. These parameters,

combined with material properties such as Young's modulus, Poisson's ratio, and friction coefficients, facilitate the computation of inter-particle interaction forces. Forces and torques are calculated using the Hertz contact model, as described in Ref. [33], with relevant formulas and physical quantities detailed in Table 1.

Figure 1 illustrates the position vector, contact point, normal vector, tangential deformation direction, velocity, and angular velocity of two ellipsoids. The formulas for computing the interaction forces and torques between particles based on these quantities are provided in Table 1. Here, $\hat{n}$ represents the normal vector at the contact point, and $\hat{t}$ denotes the unit vector along the tangential deformation at that point. The vector $\boldsymbol{r}_{ic} = \boldsymbol{r}_c - \boldsymbol{r}_i$ represents the vector directed from the center of mass of particle i towards the contact point c, and $\boldsymbol{r}_{jc}$ is similarly defined. The components of $\boldsymbol{r}_{ic}$ and $\boldsymbol{r}_{jc}$ along the normal vector are denoted by $\boldsymbol{r}_{icn}$ and $\boldsymbol{r}_{jcn}$, respectively; r_{ijn} is defined as $r_{ijn} = (\boldsymbol{r}_j - \boldsymbol{r}_i)\cdot\hat{n}$; μ_s is the sliding friction coefficient, μ_r is the rolling friction coefficient, c_t is the tangential damping coefficient, c_n is the normal damping coefficient, k_r is the rolling stiffness, and γ_r is the rolling viscosity.

Table 1. Forces and torques.

Physical quantities	Equations
Normal overlapping	δ_n
Tangential displacement vector	$\hat{\delta}_t = \boldsymbol{\delta}_t/\lvert\boldsymbol{\delta}_t\rvert$
Tangential maximum displacement	$\delta_{t,max} = \mu_s(2-v)/(2-2v)\delta_n$
Poisson's ratio	v
Effective Young's modulus	$E^* = E/(2-2v^2)$
Effective mass	$m_{ij} = m_i m_j/(m_i+m_j)$
Effective curvature	$R^* = R_i R_j/(R_i+R_j)$
Normal spring force	$\boldsymbol{f}_{cn} = \frac{4}{3}E^*\sqrt{R^*}\delta_n^{3/2}\hat{n}$
Normal viscous force	$\boldsymbol{f}_{dn} = -c_n(8m_{ij}E^*\sqrt{R^*\delta_n})^{1/2}\boldsymbol{v}_{n,ij}$
Tangential spring force	$\boldsymbol{f}_{ct} = -\mu_s\lvert\boldsymbol{f}_{cn}\rvert[1-(1-\delta_t/\delta_{t,max})^{3/2}]\hat{t}$
Tangential viscous force	$\boldsymbol{f}_{dt} = -c_t(6\mu_s m_{ij}\lvert\boldsymbol{f}_{cn}\rvert\sqrt{1-\delta_t/\delta_{t,max}}/\delta_{t,max})^{1/2}\boldsymbol{v}_{t,ij}$
Torque	$\boldsymbol{q}_i = \boldsymbol{r}_{ic}\times(\boldsymbol{f}_n+\boldsymbol{f}_t)$
Relative sliding velocity	$\boldsymbol{v}_{ij} = \boldsymbol{v}_i - \boldsymbol{v}_j + \boldsymbol{\omega}_i\times\boldsymbol{r}_{ic} - \boldsymbol{\omega}_j\times\boldsymbol{r}_{jc}$
Normal relative velocity	$\boldsymbol{v}_{n,ij} = (\boldsymbol{v}_{ij}\cdot\hat{n})\hat{n}$
Tangential relative velocity	$\boldsymbol{v}_{t,ij} = \boldsymbol{v}_{ij} - \boldsymbol{v}_{n,ij}$
Relative rolling velocity	$\boldsymbol{v}_r = -\frac{r_{icn}r_{jcn}}{r_{ijn}}\hat{n}\times(\boldsymbol{\omega}_i-\boldsymbol{\omega}_j)$
Rolling force	$\begin{cases}\boldsymbol{f}_r = \min(\mu_r f_n, \lvert\boldsymbol{f}_0^r\rvert)\hat{f}_0^r \\ \boldsymbol{f}_0^r = -k_r\boldsymbol{\xi}_r - \gamma_r\boldsymbol{v}_r\end{cases}$
Rolling torque	$\boldsymbol{q}^{rolling} = \frac{r_{icn}r_{jcn}}{r_{ijn}}\hat{n}\times\boldsymbol{f}_r$

The computation of normal and tangential forces in Table 1 follows the model employed in a previous study,[33] and the calculation of rolling force and torque utilizes a non-spherical extension[34,35] of the spherical particle model.[36,37] The relative rolling velocity $\boldsymbol{v}_r$ at the contact point, as shown in Table 1, is used to compute rolling resistance. The rolling deformation $\boldsymbol{\xi}_r$ is determined by integrating the relative velocity v_r over time, expressed as $\boldsymbol{\xi}_r = \int \boldsymbol{v}_r \mathrm{d}t$. In practical calculations, the rolling deformation at time $t+\Delta t$ is given by $\boldsymbol{\xi}_r^{t+\Delta t} = \boldsymbol{\xi}_r^t + \boldsymbol{v}_r^{t+\Delta t}\Delta t$. Here, $\boldsymbol{\xi}_r^t$ denotes the rolling deformation at time t, and $\boldsymbol{v}_r^{t+\Delta t}$ represents the relative rolling velocity at time $t+\Delta t$. It is crucial to recognize that at time $t+\Delta t$, the orientation of $\boldsymbol{\xi}_r^t$ may not align perpendicularly with the normal vector $\hat{n}$. In such cases, it becomes necessary to rotate $\boldsymbol{\xi}_r^t$ into the tangent plane and then combine it with the deformation induced by the relative rolling velocity at time $t+\Delta t$. This procedure allows for accurate determination of the rolling deformation. Following this, the rolling deformation serves as a basis for calculating the rolling force and torque. Table 1 presents the rolling force under frictional conditions. Additional insights on rolling resistance are available in the previous studies.[35,36]

Table 2. Simulation parameters.

Parameters	Values	Units
Length-unit	1	1 mm
Mass-unit	1	1 mg
Time-unit	1	1 ms
Particle density ρ	2.65	2.65×10^3 kg/m^3
Young's modulus E	5.67×10^7	56.7 GPa
Friction coefficient μ_s	0.50	0.50
Poisson's ratio v	0.2	0.2
Normal viscosity coefficient c_n	0.2	0.2
Tangential viscosity coefficient c_t	0.2	0.2
Rolling stiffness k_r	10^6	10^6 N/m
Rolling viscosity γ_r	10^3	1.0 kg/s
Rolling friction coefficient μ_r	0.1	0.1
Integration time-step	1×10^{-3}	1×10^{-6} s

To facilitate comparison with experimental results, this study utilizes the material parameters of the sample employed in the experiment,[38] detailed in Table 2. These parameters are crucial for calculating forces, torques, acceleration, and angular acceleration. The leap-frog method[39] is employed to update translational velocity and particle displacement. Addi-

tionally, an algorithm[40] is utilized to update angular velocity and displacement, ensuring high accuracy and efficiency.

Once the contact model and material parameters are defined, simulations are performed for the ellipsoidal system described by the equation $\frac{x^2}{\alpha^2}+y^2+\frac{z^2}{(1/\alpha)^2}=1$. The shape of the ellipsoid is dictated by the parameter α, which ranges between 1.1 and 2.0. The sample preparation process is illustrated using the shape with $\alpha=2.0$; other shapes are prepared in a similar manner. To eliminate the effects of boundary conditions, periodic boundary conditions were applied horizontally, and the bottom is fixed with a wall. The centers of mass of the particles are positioned randomly, and their angular displacements are also generated randomly. Particles are released under gravity with random initial velocities and angular velocities to achieve a random packing structure. The initial state of the system is illustrated in Fig. 2(a). After the system has reached equilibrium with zero translational and rotational kinetic energies under gravity, a normal stress is applied to it via a wall above. The system is then allowed to reach equilibrium again. This process is repeated until the system achieves a packed state under the given normal stress, as shown in Fig. 2(b). The normal stress σ_{zz} ranges from 100 kPa to 900 kPa.

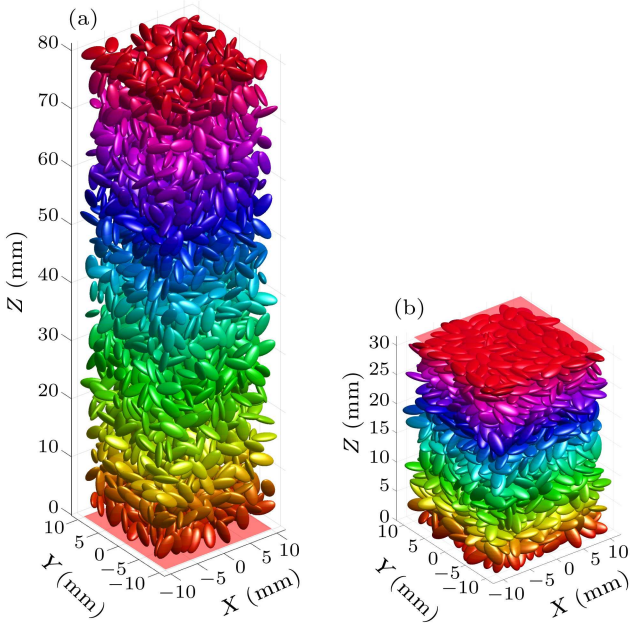


Fig. 2. Packing of ellipsoids: (a) initial state, (b) final state.

2.2. Calculation of sound velocity

Once equilibrium has been reached, vertical harmonic vibrations of the bottom wall can simulate longitudinal waves, while horizontal harmonic vibrations can simulate transverse waves. The waveforms of these waves can be determined by calculating the fluctuations in force on the upper wall, allowing for the calculation of sound velocity. To demonstrate the simulation of the sound propagation process and the calculation of sound velocity, we consider the system with $\sigma_{zz}=1$ MPa and $\alpha=2.0$ as an example. The vibration equation of the bottom wall describes a plane passing through $r_w=(0,0,0)$ with a normal vector $(0,0,1)$. The positions $r_w=(0,0,A\sin(2\pi ft))$ and $r_w=(A\sin(2\pi ft),0,0)$ represent simple harmonic vibrations of the wall in the vertical and horizontal directions, respectively. In the absence of any applied vibration, the force acting on the upper wall equals the applied stress and remains constant over time. However, when the bottom wall vibrates, the force acting on the upper wall experiences perturbations. These fluctuations in stress on the upper wall indicate the propagation of elastic waves within the system. To accurately determine the stress perturbation on the upper wall caused by the propagation of elastic waves, it is essential to record the vertical stress on the upper wall without vibration as a function of time, denoted as $F_{z0}(t)$. The program should then be rerun under identical conditions with vertical vibration applied, recording the resulting vertical stress on the upper wall as $F_{zv}(t)$. The difference over time $\Delta F_z(t)=F_{zv}(t)-F_{z0}(t)$ represents the longitudinal waveform of the elastic wave. Similarly, the transverse waveform is expressed as $\Delta F_x(t)=F_{xv}(t)-F_{x0}(t)$. The longitudinal and transverse waveforms under the conditions shown in Fig. 2(b), with a frequency of $f=20$ kHz and a displacement amplitude of $A=10^{-3}$ mm, are illustrated in Fig. 3. At $t=0$, the bottom wall begins vibrating, and there is no stress fluctuation in the vertical direction of the upper wall until $t=2.19\times10^{-5}$ s, indicating that the vibration has not yet propagated to the upper wall during this period. Afterward, the stress on the upper wall starts to fluctuate.

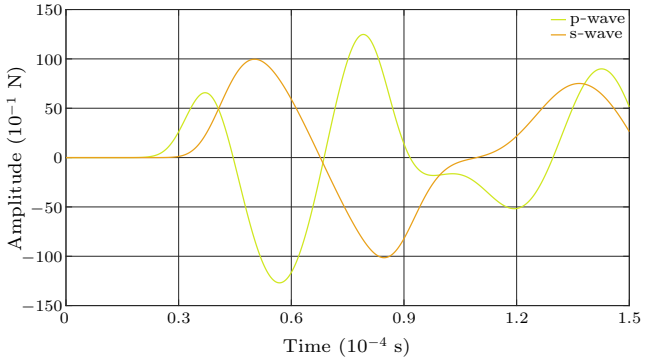


Fig. 3. Longitudinal and transversal waveforms.

The initial stress peak is observed at $t=3.72\times10^{-5}$ s, corresponding to the time required for the elastic wave to propagate from the bottom to the top of the system.[41,42] The height of the sample, which represents the distance traversed by the wave in the longitudinal direction, is 31.3213 mm. Therefore, the velocity of the wave can be calculated to be $v_{\rm p}=\frac{31.3213\ \text{mm}}{3.72\times10^{-5}\ \text{s}}=841.9717$ m/s. Using the same methodology, the transverse wave velocity is determined to be $v_{\rm s}=625.1763$ m/s. The variation of sound velocity with shape under different normal stresses is illustrated in Fig. 4.

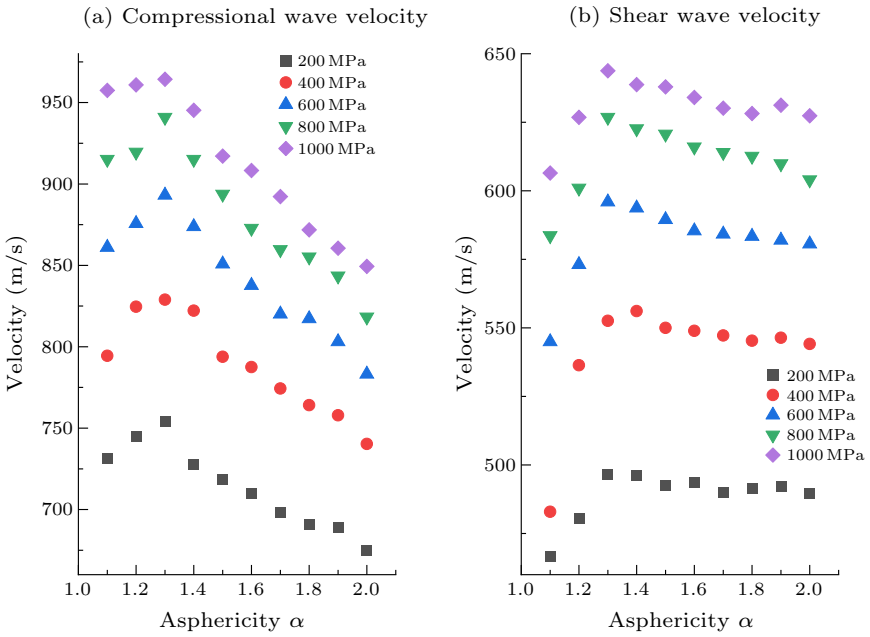


Fig. 4. Variation of sound velocity with shape under different normal stresses.

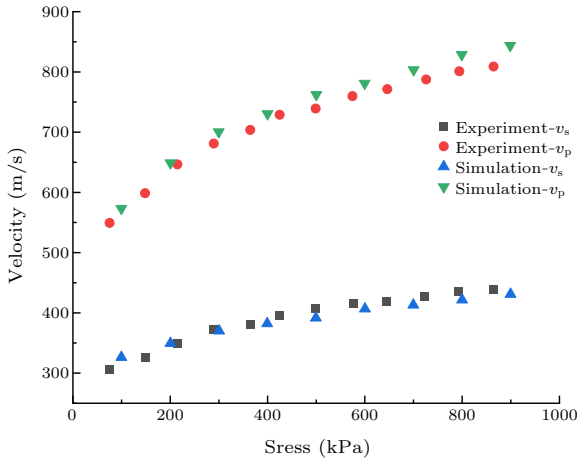


Fig. 5. Comparison of the sound velocities between simulation and experimental results.

2.3. Validation of discrete element simulation

The volume fraction and coordination number are pivotal parameters that regulate the state of particle systems and markedly influence their macroscopic mechanical properties.[43] To enhance the reliability of the simulated results, comparisons were made with experimental data from other sources. In this study, the volume fraction and coordination number for spherical particle system are 0.647 and 6.96, respectively, which are analogous to a previous work.[38] The volume fraction ϕ and coordinate number Z of maximally dense random packing of frictionless ellipsoidal system $(\frac{x}{1.3})^2+(\frac{y}{1})^2+(\frac{z}{1/1.3})^2=1$ under periodic boundary condition are 0.725 and 10.85, respectively.[44] The simulation result is similar to a previous work.[45]

To illustrate the reliability of the present method, the sound velocity of spherical particle system under different normal stresses is calculated by using the experimental parameters,[38] and the results are consistent with those of existing experiments as shown in Fig. 5.

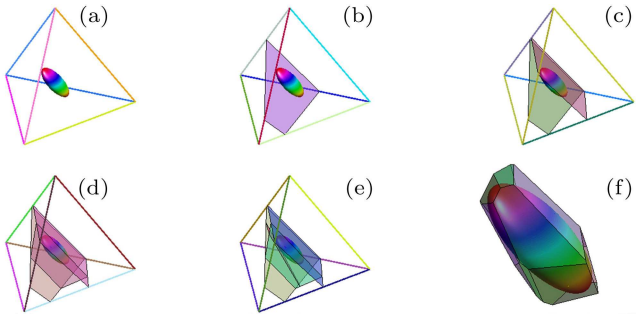


Fig. 6. Process of polyhedron generation.

2.4. Determination of the polyhedron

A clear correlation exists between the variation of sound velocity and the geometric properties of the system's polyhedra. Analyzing and determining these polyhedra can help to explain the macroscopic properties of the system. Constructing Voronoi meshes in a system of non-spherical particles is impractical. Therefore, in this study, we use polyhedra formed by tangent planes at the contact points of ellipsoids instead of Voronoi meshes to explore the relationship between polyhedral structures and sound velocity. To illustrate the determination of polyhedra, we take an ellipsoidal particle from the system with normal stress $\sigma_{zz}=1$ MPa and $\alpha=2$ as an example. The centroid of the ellipsoid is located at $\boldsymbol{X}=(-6.5790,-6.6620,19.6989)$, with an angular coor-

dinate of

$$\boldsymbol{R} = \begin{pmatrix} -0.6101 & 0.2210 & 0.7609 \\ -0.6720 & -0.6530 & -0.3493 \\ 0.4197 & -0.7044 & 0.5469 \end{pmatrix}.$$

The first step is to construct a tetrahedron of suitable size centered at the particle's center of mass, ensuring the particles are enclosed within it, as shown in Fig. 6(a). Next, we try to determine the order of dissection based on the distance from the tangent point to the center of mass, prioritizing the shortest distances. The nearest tangent plane intersects the original tetrahedron, and the section below it is removed to form a new, smaller polyhedron, as illustrated in Fig. 6(b). Figures 6(c)–6(e) demonstrate the polyhedron after the dissection of the second through fourth tangent planes. After all tangent planes have been dissected, the final polyhedron, as shown in Fig. 6(f), is achieved.

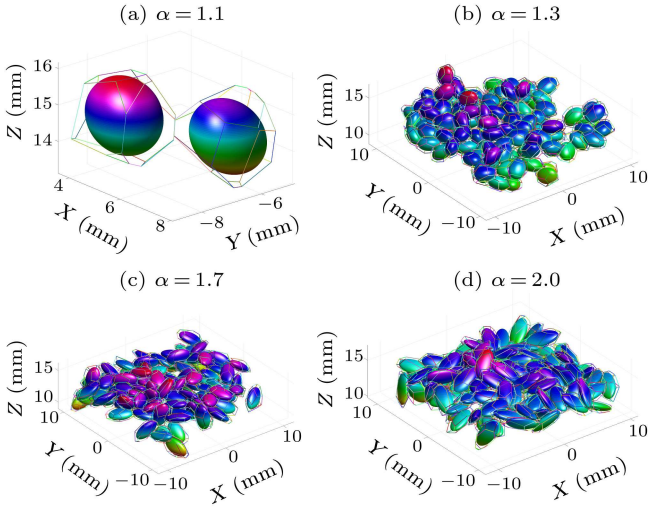


Fig. 7. The internal structure of ellipsoidal packing systems.

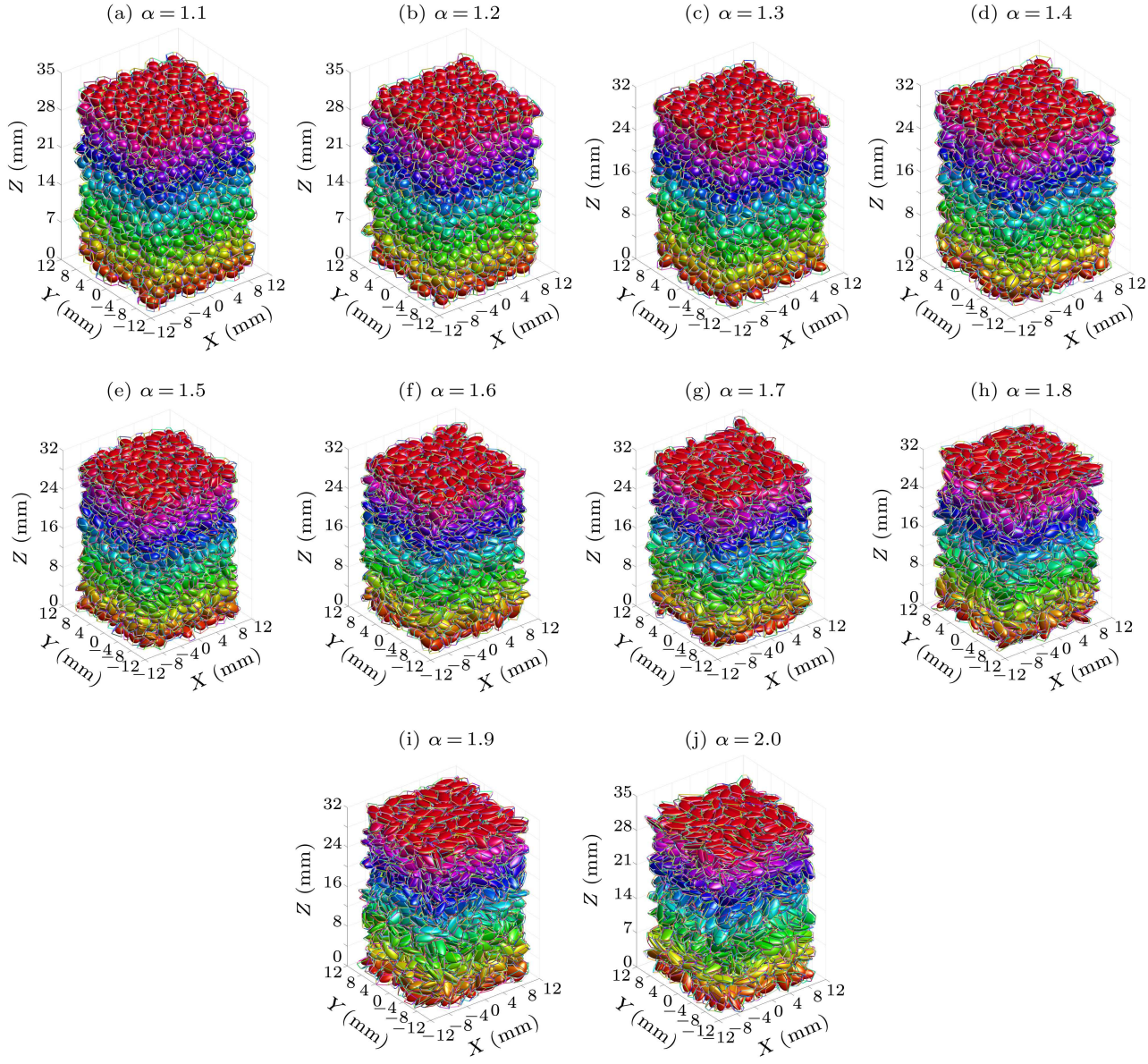


Fig. 8. The overall structure of ellipsoidal packing systems.

When two particles are in close proximity but not in contact, it is necessary to identify the potential contact point. To illustrate this process, Fig. 7(a) shows how to determine the potential contact point. The equation $(\frac{x}{1.1})^2+(\frac{y}{1})^2+(\frac{z}{1/1.1})^2=1$ represents the original size of the particles, where the two particles are not in contact. When the equation $(\frac{x}{1.1})^2+(\frac{y}{1})^2+(\frac{z}{1/1.1})^2=k>1$ is satisfied, the particles are enlarged, with the value of k gradually increasing until the two particles become tangent. At this point, the tangent point is the potential contact point. Applying a tangent plane at this point results in a unique polyhedron. The internal structure of ellipsoidal packing systems with different shapes, represented by the equation $(\frac{x}{\alpha})^2+(\frac{y}{1})^2+(\frac{z}{1/\alpha})^2=1$, $\alpha\in[1.1,\ 2.0]$, can be determined by using this method, as shown in Figs. 7(b)–7(d). The overall structures of the systems are illustrated in Fig. 8.

3. Relationship between sound velocity and polyhedral structures

Once the polyhedron is obtained, the average number of vertices, edges, faces, surface area, and volume can be calculated to determine the correlation between these quantities and the sound velocity. The number of vertices, edges, and faces, as well as the surface area and volume of the polyhedra formed by the tangential planes of the particles, vary in systems of different shapes. As shown in Fig. 9, these geometric quantities change in response to alterations in shape.

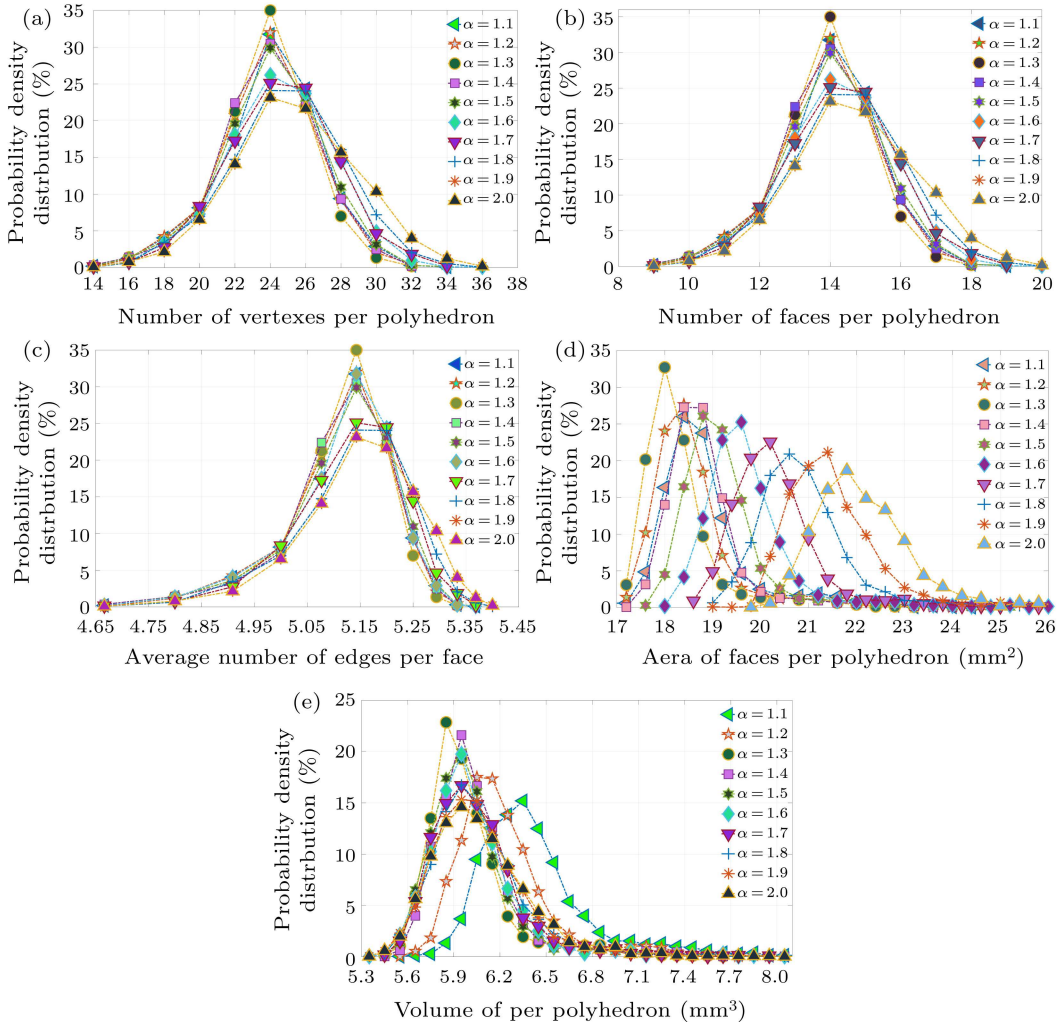


Fig. 9. Polyhedrons' topological and metric properties for different values. (a) Vertexes per polyhedron; (b) faces per polyhedron; (c) average number of edges of each polyhedron face; (d) surface areas, and (e) volumes of each polyhedron.

As shown in Fig. 9, the patterns governing the vertices, faces, edges, surface areas, and volumes of the polyhedron exhibit a consistent evolution with respect to α. Initially, these attributes decrease as α increases. However, after reaching their minimum values at $\alpha=1.3$, they steadily increase with further increments in α. For α values less than 1.6, the probability density peaks for vertices, faces, and edges are identical, with values of 24 for vertices, 14 for faces, and an average edge number of $\bar{e}=5.143$. The value $f=14$ represents the predominant peak for monodisperse systems, in accordance with the previous studies.[46,47] Similarly, the peak of the average edge number per polyhedron face, $\bar{e}=5.143$, aligns with the findings of Yi *et al.*[48]

For $\alpha\geq 1.7$, the peaks shift slightly to higher values,

reaching $v = 26$, $f = 16$, and $\bar{e} = 5.2$. The metric properties of the polyhedron, specifically its surface area and volume, follow a similar pattern. For $\alpha < 1.3$, the relationship of α to the surface area and volume is inverse; smaller α values correspond to larger surface areas and volumes. In contrast, for $\alpha \geq 1.3$, greater α values lead to smaller surface areas and volumes.

The quantities in question, whether referring to vertices, faces, surface areas, volumes of each polyhedron, or average edge numbers of each polyhedron face, show an inverse relationship with velocity. For example, the maximum velocity is observed at $\alpha = 1.3$, coinciding with the minimum values of these attributes. As these quantities increase, the velocity decreases. This inverse relationship suggests that nature tends to optimize maximum efficiency at minimal cost.

The geometric structure of polyhedra is related to both thermal and acoustic conductivity properties.[48] To ascertain the relationship between structure and sound velocity, a series of simulations were conducted. These simulations involved generating elastic waves with simple harmonic vibrations in both vertical and horizontal directions. The longitudinal and transversal wave velocities of the system were calculated using the time-of-flight method to analyze the relationship between sound velocities and the variations in the system's polyhedral points, edges, surfaces, volumes, and surface areas, for different shapes and normal stresses.

The sound velocity increases with the increase in normal stress and exhibits a rise and then a fall with the value of α under the same normal stress. The peak value occurs at $\alpha = 1.3$. Additionally, at $\alpha = 1.3$, the number of vertices, number of faces, average number of edges per face, volume, and surface area of the polyhedra are all minimal. When α is within the range (1.1, 1.3), the wave velocity increases with increasing α, accompanied by a corresponding decrease in the surface area, volume, number of vertices, and average number of edges per face of the polyhedron. Consequently, larger geometric quantities correlate with slower sound velocity. For α in the range (1.3, 2.0), the sound velocity decreases with increasing α, while the corresponding surface area, volume, number of vertices, and average number of edges per face of the polyhedron increase. This suggests that as these geometric quantities increase, the sound velocity decreases. This pattern is consistent with that observed for $\alpha \leq 1.3$.

4. Conclusion

Statistical laws for the polyhedral structure indicate that the dissected polyhedron's characteristics vary significantly with shape. At $\alpha = 1.3$, the volume, number of vertices, number of edges, and area of each face of the dissected polyhedron are smallest. The partitioned polyhedron exhibits its smallest volume, fewest vertices, and fewest edges when the maximum sound velocity is reached. Conversely, as these geometric quantities increase, the sound velocity decreases. The dissected polyhedron demonstrates pronounced acoustic conductivity properties at $\alpha = 1.3$. The correlation between the system's sound velocity and its shape aligns with the correlation between the geometry and shape of the dissected polyhedron. The porous medium structure corresponding to the polyhedron, once the particles have been removed, can serve as a reference for designing acoustic materials.

Acknowledgments

Supported by the National Natural Science Foundation of China (Grant Nos. 12262005, 11962003, and 11602062), the Postgraduate Education Reform and Quality Improvement Project of Henan Province (Grant No. YJS2024AL138), and the Graduate Education Reform Project of Henan Province (Grant No. 2023SJGLX096Y).

References

[1] Lazar E A, Lu J and Rycroft C H 2022 *Am. J. Phys.* **90** 469
[2] O'hern C S, Silbert L E, Liu A J and Nagel S R 2003 *Phys. Rev. E* **68** 011306
[3] Rycroft C H, Grest G S, Landry J W and Bazant M Z 2006 *Phys. Rev. E* **74** 021306
[4] Suikkanen H, Ritvanen J, Jalali P and Kyrki-Rajamäki R 2014 *Nucl. Eng. Des.* **273** 24
[5] Puckett J G, Lechenault F and Daniels K E 2011 *Phys. Rev. E* **83** 041301
[6] Rycroft C H, Kamrin K and Bazant M Z 2009 *J. Mech. Phys. Solids* **57** 828
[7] Panaitescu A and Kudrolli A 2014 *Phys. Rev. E* **90** 032203
[8] Guo N and Zhao J 2014 *Phys. Rev. E* **89** 042208
[9] Rieser J M, Goodrich C P, Liu A J and Durian D J 2016 *Phys. Rev. Lett.* **116** 088001
[10] Richard P, Oger L, Troadec J P and Gervois A 2001 *Eur. Phys. J. E* **6** 295
[11] Jowitt P W and Munro J 1975 *The influence of void distribution and entropy on the engineering properties of granular media.* In *Proceedings: applications of statistics and probability in soil and structural engineering, 2nd international conference* Schultze E (ed) (Essen, Germany: Deutsche Gesellschaft fúr Erdund Grundbau) pp. 365–385
[12] Kang D H, Choo J and Yun T S 2013 *Comput. Geotech.* **49** 53
[13] Kang D H, Yun T S and Evans T M 2014 *Comput. Geotech.* **59** 1
[14] Kang D H, Yun T S and Evans T M 2014 *Comput. Geotech.* **59** 1
[15] Askari R, Taheri S and Hejazi S H 2015 *AIP Adv.* **5** 097106
[16] Luchnikov V A, Medvedev N N, Oger L and Troadec J P 1999 *Phys. Rev. E* **59** 7205
[17] Baule A, Mari R, Bo L, Portal L and Makse H A 2013 *Nat. Commun.* **4** 2194
[18] Schaller F M, Neudecker M, Saadatfar M, Delaney G W, Schröder-Turk G E and Schröter M 2015 *Phys. Rev. Lett.* **114** 158001
[19] Dong K, Wang C and Yu A 2016 *Chem. Eng. Sci.* **153** 330
[20] Sadd M H, Adhikari G and Cardoso 2000 *Powder Technol.* **109** 222
[21] Lherminier S, Planet R, Simon G, Vanel L and Ramos O 2014 *Phys. Rev. Lett.* **113** 098001
[22] Liu C H and Nagel S R 1992 *Phys. Rev. Lett.* **68** 2301
[23] Chang C S and Gao J 1995 *Int. J. Non-Linear Mech.* **30** 111
[24] Hostler S R and Brennen C E 2005 *Phys. Rev. E* **72** 031303
[25] Shlivinski A and Langenberg K J 2007 *Ultrasonics* **46** 89
[26] Khidas Y and Jia X 2012 *Phys. Rev. E* **85** 051302
[27] Edwards A N, Viroulet S, Johnson C G and Gray J M N T 2021 *J. Fluid Mech.* **915** A9
[28] Tang X and Yang J 2021 *J. Mech. Phys. Solids* **157** 104605
[29] Mirghasemi A A, Rothenburg L and Matyas E L 2002 *Géotechnique* **52** 209
[30] Azéma E, Estrada N and Radjai F 2012 *Phys. Rev. E* **86** 041301

[31] Wang S, Zhuravkov M and Ji S 2020 *Soft Matter* **16** 7760
[32] Wang S and Ji S 2022 *Comput. Methods Appl. Mech. Eng.* **393** 114802
[33] Podlozhnyuk A, Pirker S and Kloss C 2017 *Comput. Part. Mech.* **4** 101
[34] Zhao C, Li C and Hu L 2018 *Physica A* **492** 181
[35] Cheng X, Li C, Peng Y and Zhao C 2021 *Granular Matter* **23** 1
[36] Luding S 2004 *Int. J. Solids Struct.* **41** 5821
[37] Luding S 2008 *Granular Matter* **10** 235
[38] Khidas Y and Jia X 2010 *Phys. Rev. E* **81** 021303
[39] Rapaport D C 2004 *The Art of Molecular Dynamics Simulation* (Cambridg: Cambridge University Press) p. 18
[40] Zhao F and Van Wachem B G M 2013 *Acta Mech.* **224** 3091
[41] Clayton C R I 2011 *Géotechnique* **61** 5
[42] Cheng H, Luding S, Saitoh K and Magnanimo V 2020 *Int. J. Solids Struct.* **187** 85
[43] Gao Q, Chen Y and Hu L 2023 *Chin. Phys. B* **32** 064702
[44] Zhao C, Zhang X, Gao Q and Li C 2022 *Powder Technol.* **404** 117460
[45] Donev A, Cisse I, Sachs D, Variano E, Stillinger F, Connelly R, Torquato S and Chaikin P 2004 *Science* **303** 990
[46] Yang R Y, Zou R P and Yu A B 2002 *Phys. Rev. E* **65** 041302
[47] Xu J Q, Zou R P and Yu A B 2007 *Granular Matter* **9** 455
[48] Yi L Y, Dong K J, Zou R P and Yu A B 2015 *Phys. Rev. E* **92** 032201